How cancer-associated fibroblasts promote T-cell exclusion in human lung tumors: a physical perspective

Joseph Ackermann[a,b], Chiara Bernard[c], Philemon Sirven[d,e], Hélène Salmon[d,e,f], Massimilano Fraldi[b,g], Martine Ben Amar[b,h]

[a]*Laboratoire Jean Perrin, Sorbonne Université, 4 Place Jussieu, 75005 Paris, France*
[b]*Laboratoire de Physique de l'Ecole normale supérieure, ENS, Université PSL, CNRS, Sorbonne Université, Université Paris Cité, F-75005 Paris, France*
[c]*Department of Civil, Environmental and Mechanical Engineering, University of Trento, Italy*
[d]*Institut Curie, INSERM, U932, Equipe Leader Fondation ARC 2018, Paris, France*
[e]*PSL Research University, Paris, France*
[f]*Icahn School of Medicine at Mount Sinai, New York, NY, USA*
[g]*Department of Structures for Engineering and Architecture, University of Naples "Federico II", Italy*
[h]*Institut Universitaire de Cancérologie, Faculté de médecine, Sorbonne Université, 91 Bd de l'Hôpital, 75013 Paris, France*

Abstract

The tumor stroma is a tissue composed primarily of extracellular matrix, fibroblasts, immune cells, and vasculature. Its structure and functions, such as nutrient support and waste removal, are altered during malignancy. Tumor cells transform the fibroblasts into cancer-associated fibroblasts, which have an important immunosuppressive activity, on which growth, invasion and metastasis depend. These activated fibroblasts appear to prevent immune cell infiltration into the tumor nest, thereby promoting cancer progression and inhibiting T-cell-based immunotherapy. To better understand the biophysics of the tumor stroma and predict the evolution of cancer cells, we measure the density of differenT-cell types in the stroma using immunohistochemistry stained tumor samples from lung cancer patients. We then incorporate these data, as well as known information on cell proliferation rates and relevant biochemical interactions, into a minimal biomechanical model. We quantify the complex dynamics between species as a function of the system properties, highlighting the inefficiency of immune cells and the fundamental role of activated fibroblasts. A spatio-temporal approach of the inhomogeneous environment and non-uniform cell distributions explains the fate of lung carcinomas. The model reproduces that, while cancer-associated fibroblasts act as a barrier to tumor growth, they also reduce the efficiency of the immune response. Our conclusion is that number of outcomes exist as a result of the competition between the characteristic times of cancer cell growth and the activity rates of the other species. For example, simulations reveal scenarios where tumor nests persist despite the presence of an efficient immune response.

1. Introduction

Cancer results from the malignant transformation of cells due to genetic changes or damage that causes cells to grow and spread in an abnormal and uncontrolled way. Mutated cells can form solid tumor tissue at specific sites and spread to distant regions of the body through a process known as metastasis. The growth, development and response to drugs and therapies of tumor masses are highly dependent on biophysical environmental conditions. These involve a not fully understood crosstalk between cancer cells and the surrounding stroma, which consists of cancer-associated fibroblasts, vessels and immune cells embedded in the extracellular matrix. Indeed, the tumor-stroma ratio turns out to be an independent prognostic factor, with a large proportion of stroma leading to a worse prognosis [1]. In this paper, we focus on modeling tumor-stroma interactions in lung cancer which is one of the most common and deadly cancers, with more than 2.2 million new cases diagnosed and 1.8 million deaths worldwide in 2020, and more specifically in non-small cell lung carcinoma (NSCLC) which accounts for the vast majority of lung cancers (85%) [2]. The majority of cells that make up the stroma are fibroblasts and macrophages. Both types are affected and reprogrammed by cancer cells and have been shown to act as tumor promoters and tumor suppressors, depending on the stage of tumor progression and of its mutational status [3, 4]. As cancer progresses, tumor cells often transform surrounding healthy fibroblasts into cancer-associated fibroblasts (CAFs) which, similar to a wound healing context, produce higher levels of extracellular matrix (ECM) as well as growth factors and cytokines that affect the recruitment of immune, vascular and epithelial/cancer cells [5].

Experimental observations and evidence of the mutual interactions between cancer cells, the immune response and cancer-associated fibroblasts suggest that a multi-physical model of the tumor microen-

vironment (TME), including molecular and spatial dynamics, could be highly beneficial in understanding and predicting the complex evolution of tumor growth and progression, and thus represent a critical step in improving T-cell-based therapies. A recent paper by Mukherjee *et al.* analyzed the spatial dynamics of infiltrating splenocytes in an aggregate of cancerous melanocytes using experimental data obtained *in vitro* [6]. Their conclusion is that a strong persistent random walk and contact energies are important for the ability of T-cells to infiltrate the tumor. However, to the best of our knowledge, there are no approaches in the current literature to model the dynamics behind human lung tumor proliferation due to the role of CAFs in excluding T-cells from the nest. Here, we propose a model for NSCLC tumors to describe the dynamic interplay between cancer cells, T-cells and fibroblasts in their resting and activated states, incorporating the most relevant interactions within the human tumor microenvironment.

To this end, we briefly review the literature on the interactions between different tumor components, including quantitative information on their composition. In particular, we base our model on data extracted from tumor microenvironment immunohistochemistry (IHC) staining performed on a large cohort of human NSCLC tumor samples, which allowed us to calibrate our model and make it consistent with actual data [7] (Section 2). We then build the theoretical description in two steps. In a first step, we ignore any spatial organization and model the proliferation and activation phenomena alone, while introducing a pressure-like term to avoid excessive proliferation and jamming insistent with the actual evidence. This leads to a nonlinear dynamical system for the cell concentrations (Section 3). Careful analysis of this dynamical system yields a stable steady state in which T-cells become inefficient against tumor survival for a given set of parameters. In a second step, we enrich the model by considering the spatio-temporal evolution of tumor growth through a continuum mathematical variational approach for cell mixtures based on the Rayleighian principle. Finite element-based simulations in two-dimensional space demonstrate the ambiguous activity of cancer-associated fibroblasts (CAFs) in regulating cancer cell proliferation and invasion (Section 4). In the Appendix, further details about the results of numerical simulations are provided to show how the proposed dynamical system is able to capture different evolutionary and tumor fates depending on the role played by the species, their initial conditions, as well as the shapes and distributions of the regions occupied by cells.

2. Lung Cancer Microenvironment

Modeling the tumor environment requires a deep understanding of the interactions between the various components, such as cells of different types, soft materials and fibers, as well as fluids and diffusing molecules. These interactions are summarized in section 2.1. Next, in section 2.2, we present data on the density of the differenT-cell types in the TME. Indeed, our continuous approach requires biological data *in vivo*, variable between different patients and different tumor areas, and also evolving over time within the tumor. Therefore, after a review of the available values found in the literature, we performed direct measurements from samples stained by multiplex IHC to study the composition of fibroblasts and distribution of T-cells in human NSCLC tumors in situ [7].

2.1. Interactions Between TME Components

Almost all tissues contain a population of fibroblasts that provide the tissue architecture, and serve as sentinels for tissue dysfunction. When a solid tumor grows, quiescent or progenitor lung fibroblasts activate an initial wound healing response with increased ECM and growth factors (cytokine) production and upregulation of activation markers such as FAP [8]. Due to mechanotransduction and/or biochemical signals from tumor or immune cells, CAFs often increase their level of contractility, which affects the maintenance of the tumor stroma [9]. CAFs are characterized by their increased mobility, proliferation, and ECM remodeling and, unlike wound-associated fibroblasts, they seem to undergo poorly reversible activation in absence of an appropriate therapy [10–13]. The diversity of this population, resulting from phenotypic modifications, explains their diverse functions and localizations in the stroma, close or distant from the tumor nest [7, 14].

Activated fibroblasts produce fibers that act as a mechanical barrier around the tumor, impeding the movement of immune cells and limiting the interaction between cytotoxic T-cells and cancer cells [15, 16]. However, by creating such a barrier around tumors, CAFs may also prevent the spread of cancer, as mechanical stress can reduce cell spreading and promote cell apoptosis [17, 18]. In addition, biochemical factors expressed by CAFs also help to modify the phenotype of T-cells or inactivate their cytotoxic capacity [19, 20]. Thus, CAFs have an ambiguous role as tumor promoters, inhibiting T-cell invasion into the nest, and as tumor suppressors, limiting the cancer growth and giving rise to an immune-excluded tumor (Fig. 1B), that is less proliferative than a free-growing tumor (Fig. 1A). Failure to confine the tumor induces high levels of cytotoxic T-cell infiltration, creating a hot tumor (Fig. 1C). Therefore, one aim of this study will be to predict susceptibility of a tumor to T-cell infiltration according to the scheme given in (Fig. 1).

In the context of non-small cell lung carcinoma (NSCLC), the recruitment of CD8+ T-cells seems to be modulated by a specific tumor-associated antigen present on the surface of the cancer cells [21]. In particular, in the family of inflammatory proteins, also

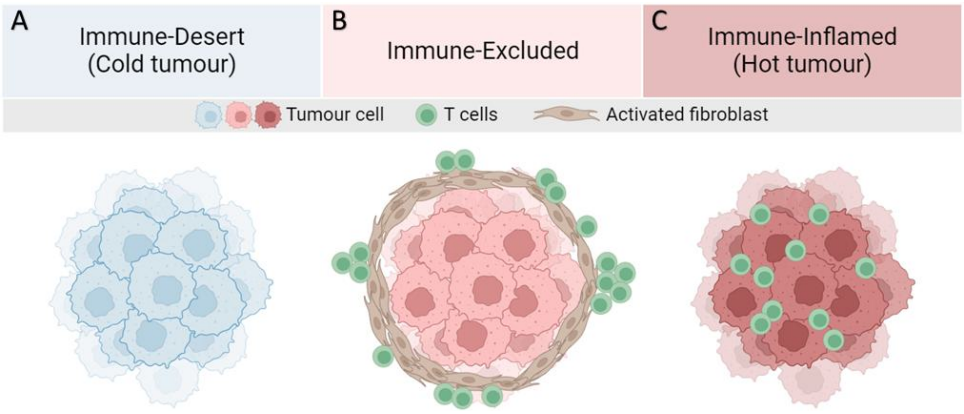

Figure 1: Major T-cell infiltration patterns observed in solid tumors. **A**: Lack of tumor antigen, inadequate priming, defects in antigen presentation and/or lack of presentation, and/or lack of T-cell-attracting chemokines result in the absence of T-cells in the tumor. **B**: Presence of T-cells in invasive margins but absent in the tumor bed. Immune evasion may be due to stromal barriers, lack of chemokines, aberrant vasculature, or hypoxia. **C**: High degree of T-cell infiltration forms a hot tumor.

called cytokines, Interlukin-6 (IL6) seems to stimulate the infiltration of $CD8^+$ [22]. The origin of $CD8^+$ T-cells that infiltrate the tumor are diverse, as they differentiate from both circulating and tissue-resident precursors [23]. However, infiltration does not imply that the immune response is efficient. In fact, an immunotherapy such as anti-PD1/PDL1 antibodies is often needed to boost the response of these T-cells. Chemical factors also play an important role in attracting T-cells via chemotaxis such as the chemokines produced by dendritic cells or cancer cells [24]. The absence of such chemicals leads to the formation of the so-called immune-desert tumor (Fig. 1A).

2.2. Lung TME Composition

For a quantitative modeling, it is crucial to use biologically well-identified data on the composition of both the tumor and the stroma. Therefore, we survey the literature to build a quantitative view for the composition of the TME. We recapitulate these values in Table. 1. However, human data show a great diversity depending on many factors such as tumor edge, patient age, non-cancer health status, but also on the method of analysis. The fibroblast population in the stroma, which is very heterogeneous and not easy to identify, is the best example. In particular, although fibroblasts are often considered to be a major component of the stroma, they are only found in small proportions in scRNA-seq with 10X single-cell systems, which may be rather surprising. This situation is well known and may be due to tissue digestion processes, to the fact that part of the stroma is not extracted with the tumor nodule, and to a lower efficiency of 10X single-cell systems for fibroblasts. Another caveat is that identifying the surface fraction of cells by staining can be very different from counting individual cells. In fact, cell types can vary greatly in size. For example, lung cancer cells can be between 13-18 μm [36], fibroblasts $\sim$ 16 μm [37], and T-cells between 5-10 μm [38], resulting in volumes and projected areas that can be 10 times smaller for T-cells compared to fibroblasts and cancer cells. Moreover, in some studies, authors look at well-characterized zones of enrichment for the different species (tumor nest, fibrotic areas), and do not consider each cell type *per se* [25, 26]. Despite these remarks, cancer cells, T-cells, and macrophages (fibroblasts are underestimated as mentioned above) appear to be a significant part of the TME. The limitations of using data coming from the literature led us to perform our own measurements. In this study, we analyzed data from 13 patients with lung squamous cell carcinoma (LUSC) and 22 patients with lung adenocarcinoma (LUAD), based on a recent publication by some of the present authors [7]. In this previous study, different fibroblast types were identified using multiplex IHC imaging. Tumor islets were stained with keratin, T-cells with CD3 and fibroblasts with αSMA, FAP and ADH1B. The coverage was evaluated for each fibroblast type and the total fibroblast coverage corresponds to the sum of these different coverages. Here, in the case of LUSC, we found that fibroblasts (composed of 6% ADH1B, 37% $FAP^+\alpha SMA^-$, 25% $FAP^+\alpha SMA^+$, 31% $FAP^-\alpha SMA^+$) occupy 35% of the stroma with a TSR of 1.29. In LUAD, these proportions were partly modified: fibroblasts (composed of 48% ADH1B, 18% $FAP^+\alpha SMA^-$, 7% $FAP^+\alpha SMA^+$, 26% $FAP^-\alpha SMA^+$) occupy 31% of the stroma, with a TSR of 1.07. The fibroblasts most responsible for T-cell exclusion are shown to be FAP^+ αSMA^+ [7]. In Fig. 2.2, we compare two LUSC microenvironments. In the top one, $FAP^+\alpha SMA^+$ are lining the tumor (Fig. 2(a),2(c), 2(d)), and T-cells are excluded from it (Fig. 2(b)). On the contrary, in cases where no $FAP^+\alpha SMA^+$ are observed, fibroblasts are homogeneously distributed in the stroma (Fig. 2(e),2(g), 2(h)), and T-cells infiltrate the tumor (Fig. 2(f)).

Ref	Method	Sample	Cancer cells	T-cells	Fibroblasts	Macrophages	TSR
[25]	Staining	LUAD	>25		>20		0.3
[26]	Staining	LUAD	67		>6.5		2.6
[27]	scRNA-seq	NSCLC		55 (S)	4 (S)	15 (S)	
[28]	scRNA-seq	SCLC	76				
[29]	scRNA-seq	LUAD	33	19.5	~ 6	20.4	
[30]	scRNA-seq	LUAD	<12	42.6	~ 1	12.2	
[31]	scRNA-seq	NSCLC	<22.7	16	8	23	
[32]	scRNA-seq	mixed types	19.9	28.1	~ 2	27.5	
[33]	scRNA-seq	LUAD	16.4	30	~2	18.4	
[34]	scRNA-seq	LUAD	12	7.5			
[5]	Staining	NSCLC			75 (S), ~0 (TN)		
Present	Staining	LUAD	47±13		31±17 (S), ~0 (T)		1.07±0.68
Present	Staining	LUSC	54±9		35±12 (S), ~0 (T)		1.29±0.51

Table 1: scRNA-seq: single-cell RNA seq. (CS): Cell Suspension, (SCLC): Small Cell Lung Cancer, (NSCLC): Non Small Cell Lung Cancer, (LUAD): Adenocarcinoma, (SSN): Sub-Solid Nodule. (S): stroma region. (T): tumour nest region. (ST): Stroma+tumour nest region. (TSR): tumour stroma ratio. Data for ref.[28–32] were extracted from [35].

3. Dynamic Modeling in the Lung Cancer TME

Our theoretical and numerical analyses consist of two steps. In a first analysis, we examine only the dynamics of an ecological system in interaction in order to evaluate the physical parameters that quantify these interactions and how the dynamics depend on them. Spatial constraints are represented by a pressure term avoiding overcrowding. We present this approach step by step in order to set the parameters one by one, highlighting the physical importance of each choice through stability analyzes of the system. The second step is the spatial description of the tumor growth in Section 4.

3.1. Dynamical System for Immune and Cancer Cells in Interaction

As we saw in the previous section, the complexity of the microenvironment makes the role of the immune system unpredictable and likely highly dependent on the tumor being studied. In the case of lung tumors, the immune system is triggered as the carcinoma expands, but T-cells may be excluded from the tumor nest by activated fibroblasts. Therefore, the goal of this work is to physically and quantitatively understand the process of T-cell exclusion from the tumor mass in the simplest way possible, and to explore different possible scenarios.

We focus on the interaction between differenT-cell types in the case of the NSCLC. We consider a closed system including the cancer cells, T-cells, non-activated fibroblasts (NAFs), cancer-associated fibroblasts (CAFs) and healthy cells with the extracellular medium. Diffusive signaling molecules are not explicitly introduced: their production by one cell type and their effect on another cell type is modeled as a direct interaction between the two. For example, the attraction of T-cells to cancer cells by chemotaxis is introduced as a source term proportional to the product of the two concentrations T and C in the T-cell equation (see below Eq. 2). We also hypothesize that the main difference between the NAFs and the CAFs is the fiber production of the latter, which prevents T-cells from infiltrating the tumor. Furthermore, we do not consider in our model that the transformation of NAFs into CAFs by cancer cells is reversible. All these cells have the same mass density and the sum of their mass fraction satisfies the relationship $\mathcal{S} = C + T + F_{NA} + F_A = 1 - N$, where the mass fraction of NSCLC cells is represented by C, T-cells by T, quiescent or non-activated fibroblasts NAFs by F_{NA}, activated fibroblasts CAFs by F_A and normal healthy cells associated with the extracellular medium by N. Note that N, as the intercellular fluid, are not active components and therefore do not appear in the following equations. We do not model here the recruitment of macrophages to better highlight the competing mechanisms related to the sole role of T-cells and CAFs in the tumor mass development. With this in mind, we write an evolution equation for each component of the system: $dX/dt = \Gamma_X$, where Γ_X corresponds to a source term modeling the proliferation, death, differentiation, or fluxes into/out of the system under study. The source terms for each species are described in detail below.

The dynamics of the cancer cells is driven by their proliferation, controlled by a growth rate coefficient α_C, and limited by a death rate $\tilde{\delta}_C$. It takes into account the population pressure caused by self-inhibition as well as by the inhibition of the other species. In the following, we will choose α_C^{-1} as the unit of time, and all coefficients introduced in the following will be pure constants without unit, so that $\tilde{\delta}_C = \alpha_C \delta_C$. In addition, cytotoxic T-cells, eliminate cancer cells if their anti-tumor activity is not inhibited by the activated fibroblasts (although they do not remove T-cells from the mixture). This process is quantified by the cytotoxic coefficient δ_{CT}, and by the coefficient of T-cell inhibition by CAFs δ_{TF}. With these assumptions, the

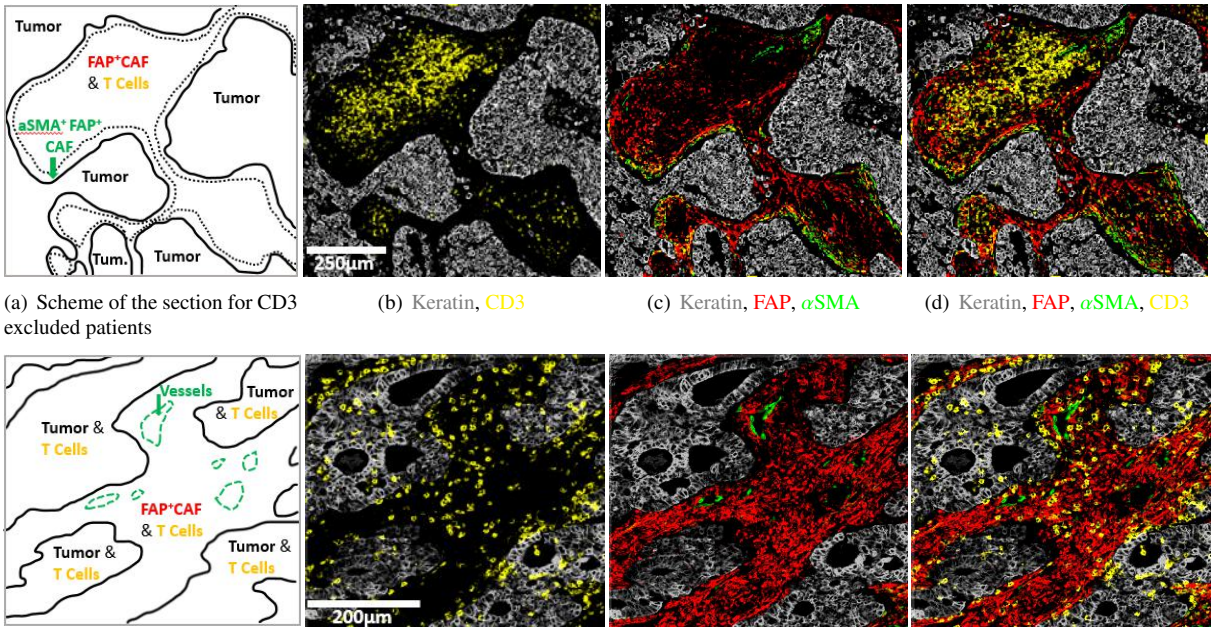

(a) Scheme of the section for CD3 excluded patients (b) Keratin, CD3 (c) Keratin, FAP, αSMA (d) Keratin, FAP, αSMA, CD3

(e) Scheme of the section for CD3 infiltrated patients (f) Keratin, CD3 (g) Keratin, FAP, αSMA (h) Keratin, FAP, αSMA, CD3

Figure 2: Staining was performed by multiplex IHC. FFPE NSCLC sections were stained for Keratin (gray), CD3 (yellow) and fibroblast markers αSMA (green), FAP (red). **2(a)-2(d)**: CD3 excluded patient showing CD3+ cell exclusion from tumor nests, CD3+ cells are localized in the center of the stroma (2(b)) and dense αSMA staining at the tumor border are associated with a decrease of CD3+ cell abundance (2(c)). The green arrow highlights border regions with contractile fibroblast barrier αSMA+FAP+ and low CD3+ cells. **2(e)-2(h)**: CD3 infiltrated patient showing CD3+ infiltration in the tumoror islets (2(f)) and FAP+ staining throughout the stroma (2(g)). The green arrow shows αSMA+ staining on vessels.

dynamics of the cancer cell population can be read:

$$\frac{dC}{dt} = C - \frac{\delta_{CT} CT}{1 + \delta_{TF} F_A} - \delta_C C\mathcal{S}, \tag{1}$$

Although proliferation of cytotoxic T-cells has been observed, we do not consider proliferation in our study as we focus on their ability to infiltrate the tumor. Therefore, their only source comes from their attraction towards cancer cells, which occurs at a recruitment rate of $\alpha_{TC}C$, while species inhibition limits their development:

$$\frac{dT}{dt} = \alpha_{TC}C - \delta_T T\mathcal{S}. \tag{2}$$

Fibroblasts are the key regulators of tumor immunity and progression. Their dynamics involve a recruitment of non-activated fibroblasts α_{NA} whose role is to maintain an adequate supply given by α_{NA}/δ_{NA} in healthy tissue, i.e. in the absence of cancer cells, and a death rate due to the pressure exerted by the cells and controlled by δ_{NA}. NAFs are attracted to the tumor nest at a rate $\alpha_{NA,C}C$ by the cancer cells that activate them to become CAFs. This process is accounted by introducing a specific transformation rate controlled by the plasticity coefficient K_A, so that the dynamic equation for NAFs reads:

$$\frac{dF_{NA}}{dt} = \alpha_{NA} + \alpha_{NA,C}C - K_A F_{NA} C - \delta_{NA} F_{NA}\mathcal{S}. \tag{3}$$

Thus, the dynamics of the CAFs is purely determined by the transformation of the NAFs and by the pressure through δ_A, which leads to:

$$\frac{dF_A}{dt} = K_A F_{NA} C - \delta_A F_A \mathcal{S}. \tag{4}$$

Therefore, the role of fibroblasts in human lung carcinoma can be investigated by studying the interplay between cancer cells and the TME. The interactions discussed above are described by 11 parameters and lead to a system of 4 coupled nonlinear differential equations concerning 4 unknowns. Within this framework, we proceed to the estimation of the parameters and the steady states of the system.

3.2. Model Parameters and Fixed Point Analysis

When all the parameters vary, the steady states or the equilibrium points of the dynamics can be quite impractical, so we start by assuming that all the coefficients at the origin of a pressure are equivalent: $\delta = \delta_C = \delta_T = \delta_A = \delta_{NA} > 0$. This reduces the number of independent parameters to 7. Fixed points are obtained by setting the time derivatives in Eqs. (1)-(4) to 0 which gives the long term behavior when the system reaches equilibrium.

In order evaluate the values of the parameters in Eqs. (1)-(4), we study different simplified situations that can be reproduced in experiments *in vitro* or

in controlled experiments *in vivo*. We will start by analyzing the case of cancer cells alone and we will successively add all the other cell types with fractions C, T, F_{NA}, F_A.

3.2.1. Cancer and T-cells

The dynamic evolution of cancer cells alone is limited to: $dC/dt = C - \delta C^2$. This equation leads to two equilibrium fixed points: $C = 0$ and $C = \delta^{-1}$ and only the second one $C = \delta^{-1}$ is stable. For the mass fraction C to be in the interval $[0, 1]$, it is $\delta \geq 1$. When cancer cells are isolated from other active cellular components, they are expected to invade the system or to be its major component, leading to a cancer death rate of $\delta \sim 1$. Note that this case is well adapted to lung tumor nests.

We now examine the interaction between T and cancer cells in the nest in the absence of fibroblasts (so $F_{NA} = F_A = 0$) and the relevant parameters scaled by δ are δ_{CT} and α_{TC}. Then, we study the equilibrium regime:

$$\begin{cases} \frac{dC}{dt} = 0 = C - \delta_{CT} CT - \delta C(C + T), \\ \frac{dT}{dt} = 0 = \alpha_{TC} C - \delta T(C + T). \end{cases} \tag{5}$$

There are three equilibrium solution pairs $\{C, T\}$, including the trivial one: $\{0, 0\}$. To analyze whether the solutions found are physically relevant ($0 \leq C, T \leq 1$) and dynamically stable, we estimate possible scalings for the two parameters, focusing on an effective immune response against cancer. For efficient elimination of cancer cells by T-cells, the killing rate δ_{CT} must be much larger than the natural death rate δ, so we introduce a small parameter $0 < \epsilon < 1$, so that $\delta_{CT} = \delta\epsilon^{-1}$. We also assume that the T-cell recruitment is slow compared to cancer cells, which means that $\alpha_{TC} = a_0\epsilon$, where a_0 being of order one. So the only stable solution is thus $\{C_+, T_+\} = \{\epsilon/((a_0 - 1)\delta), \epsilon/\delta\}$ where $a_0 > 1$. So, even if the inflammation level is low, resulting in a small number of T-cells, the immune action on the cancer cells remains efficient.

3.2.2. Role of activated fibroblasts on T-cells

Fibroblasts play an active role in the exclusion of the T-cells from the tumor nest. Therefore, we consider fixed points corresponding to an ensemble $\{C, T, 0, F_A\}$ in order to obtain a good estimate for the killing rate δ_{TF}, responsible for the marginalization of the T-cells and subsequently of the increase of cancer cells at a fixed volume fraction of fibroblasts. For simplicity, we first assume that F_A is constant, which leads to the dynamical system:

$$\begin{cases} \frac{dC}{dt} = 0 = f_0 C - \Delta_{CT} CT - \delta C(C + T), \\ \frac{dT}{dt} = 0 = \alpha_{TC} C - \Delta_F T - \delta T(C + T), \end{cases}$$

where $f_0 = 1 - \delta F_A$, $\Delta_{CT} = \delta_{CT}(1 + \delta_{TF} F_A)^{-1}$ and $\Delta_F = \delta F_A$. There are four solution pairs. We use the scaling of the two parameters already established in the previous paragraph: $\delta_{CT} = \delta\epsilon^{-1}, \alpha_{TC} = a_0\epsilon$. We also assume that the inhibition of the T-cells may counteract their cytotoxic effect on cancer cells, i.e. $(1+\delta_{TF} F_A)^{-1} \sim \epsilon$, when activated fibroblasts are abundant $F_A = \delta^{-1} f_a$. This results in $\delta_{TF} = d_0\delta\epsilon^{-1}$. The only stable equilibrium solution is $(C_+, T_+) = (f_0\delta^{-1} + O(\epsilon), O(\epsilon))$, where the notation $O(\epsilon)$ denotes a quantity whose order of magnitude is ϵ. Hence, our model confirms that when the fibroblasts inactivate the T-cells, they favor the cancer cell population.

3.2.3. Residual Fibroblasts in Healthy Tissue

In healthy tissue, most of the fibroblasts are in a quiescent state and are not activated in the absence of pathologies such as wounds, allergic reactions or cancer cells. Therefore, in such tissues, for a quiescent fibroblast population, the density of F_{NA} is the equilibrium solution of the equation $dF_{NA}/dt = 0 = \alpha_{NA} - \delta {F_{NA}}^2$. The parameter α_{NA} represents the net influx of fibroblasts into the tissue. If the fraction of non-activated fibroblasts decreases over time ϵ^2, then $\alpha_{NA} \sim \delta\epsilon^4$ can be inferred with a value of the order of 10^{-4}.

3.2.4. Fibroblast Plasticity

Fibroblast elasticity is the phenotypic change responsible for T-cell inhibition and for more active fiber production. Cancer cells drive this transformation of the current population F_{NA} into F_A. This process is quantified by the constant K_A. We first estimate that the fibroblast population is comparable to the cancer cell population when they are alone, which leads to: $F_{NA} = f_n\delta^{-1}$. Replacing: $\delta_{CT} = \delta\epsilon^{-1}, \alpha_{TC} = a_0\epsilon$, $\delta_{TF} = d_0\delta\epsilon^{-1}$, it reads:

$$\begin{cases} \frac{dC}{dt} = C - \frac{\delta\epsilon^{-1} CT}{1+d_0\delta\epsilon^{-1} F_A} - \delta C\mathcal{S}, \\ \frac{dT}{dt} = a_0\epsilon C - \delta T\mathcal{S}, \\ \frac{dF_A}{dt} = K_A f_n C/\delta - \delta\mathcal{S}. \end{cases} \tag{6}$$

Because of the effect of the fibroblasts on the T-cells, they have little effect on the cancer cells, so that cancer cell proliferation is little affected. At equilibrium, with $F_{NA} = f_n/\delta$, this leads to $C \sim \delta^{-1}$, $T \sim \epsilon\delta^{-1}$. The equation for T gives $F_A \sim a_0\delta^{-1}/d_0$. This means that the activated fibroblasts must be relatively abundant to fully inhibit the activity of the T-cells. It follows that the plasticity parameter in ϵ is of low order, since the non-activated fibroblasts are maintained at a high density: $K_A \sim \delta$.

3.2.5. Tumor Fibroblast Attraction

In this last step, we want to determine the parameter that controls the attraction of the fibroblasts to the tumor. To do this, we write $K = k\delta$ in the entire system of equations, which we rewrite according to the

previous findings:

$$\begin{cases} \frac{dC}{dt} = C - \frac{\delta\epsilon^{-1}CT}{(1+d_0\delta F_A)^{-1}} - \delta C\mathcal{S}, \\ \frac{dT}{dt} = a_0\epsilon C - \delta T\mathcal{S}, \\ \frac{dF_{NA}}{dt} = \delta\epsilon^4 + \alpha_{NA,C}C - k\delta F_{NA}C - \delta F_{NA}\,\mathcal{S}, \\ \frac{dF_A}{dt} = k\delta F_{NA}C - \delta F_A\mathcal{S}. \end{cases} \tag{7}$$

Then, we look for solutions of the type: $\{C, T, F_{NA}, F_A\} = \delta^{-1}\{c_0, t_0\epsilon^2, f_{NA}, f_A\}$. The order of magnitude of the attraction parameter is then $\alpha_{NA,C} \sim 1$.

In the next section, we summarize all the scaling laws, according to the obtained results and present different scenarios related to the definition of the tumors, given in Fig.1.

3.2.6. Numerical study of cell population dynamics

The dynamics of each cellular component of the mixture can be systematically studied according to the full set of parameters summarized in Table 2, with the corresponding orders of magnitude. Some of them can be considered as fixed in the system, i.e. they do not vary significantly between the different tumors in the phenomena studied. This category includes δ^{-1}, the inverse of the free tumor cell density, and α_{NA}, the NAF attraction parameter to healthy tissue. The other parameters can be studied as control parameters.

The simulated time-dependent densities of each cell type are displayed in Fig. 3 for different sets of parameters in the system of equations in Eqs. (1)-(4). At time $t = 0\,\mathrm{h}$, we assume small mass fractions of cancer cells, T-cells, activated and quiescent fibroblasts. Over time, the particular choice of a quadratic model allows the dynamics to reach a plateau for each cell type, confirming the stability of the fixed points found in Section 3.2.

In the case of an immune-desert tumor, i.e. when T-cells are not attracted to the tumor nest or are unable to penetrate it(Fig. 3(a),3(c)), cancer cell growth is not limited by the immune response. However, this growth saturates when it reaches a steady state controlled by δ.

If the T-cells are efficient, the tumor is said to be immune-inflamed and several scenarios can be discussed. Their response is triggered by the proliferation of cancer cells. Thus, in the absence of CAF inhibition, T-cells slow tumor growth, without however killing all cancer cells (Fig. 3(d),3(e),3(f)). In contrast, in the immmune-excluded tumor, CAFs impede the T-cell response and thus indirectly promote cancer cell growth, as observed in Fig. 3(b).

In conclusion, the dynamic equation system, limited to 4 cell types, recapitulates the different possible scenarios that could evolve according to the interaction between cancer cell growth, T-cells and fibroblasts in lung adenocarcinoma. However, it does not provide information about the morphology of the tumor and of the local composition of its microenvironment. In addition, it poorly represents the structure of the tumor, which is divided into a nest, a cancer-associated stroma, and a healthy stroma.

For these reasons, we now extend our model and present the spatio-dynamical model that we use to study the different cases mentioned above in more detail.

4. Spatio-Temporal Behavior of Tumor Growth

Spatial study is an important tool in cancer diagnosis and the shape of tumors reveals the aggressiveness of cancer cells and the role of their microenvironment [39–44]. Similarly, the localization of immune cells in the tumor environment [6], as well as proliferating and pre-metastatic cells often found in niches, are active areas of research in oncology and a valuable support for clinical prognosis [45–47].

In the previous section, we described our cell mixing through the global time evolution given by a dynamical system. Here, we aim to complete the modeling by considering the spatial heterogeneity of the interplay between fibroblasts, T-cells and cancer cells and its consequences for tumor cell localization and proliferation. We first present the mixture model [43, 48], which is able to incorporate the spatial distribution and evolution of active cells leading to a set of partial differential equations that we solve with the finite element (FEM) software COMSOL Multiphysics [49]. As in the previous section, we consider 4 differenT-cell types namely cancer cells, T-cells, activated and non-activated fibroblasts, with different attraction properties. A component that does not play an active role in the mixture is also added via an inactive N fraction. It concerns the intercellular fluid, the healthy cells and the dead cells. This last component is also a source of material, for the proliferation of cancer cells. Each component is described by a local mass fraction ϕ_i, a velocity $\mathbf{v}_i$, and a proliferation/death term Γ_i. With ϕ and Γ denoting generic quantities that are now space and time dependent. More specifically, ϕ_i corresponds to the local value of C, T, F_A, F_{NA} introduced in the previous sections and $\phi_0 = 1 - \sum_{i\neq 0}\phi_i$ represents N. Γ_i is the growth rate of each component, which is now space and time dependent (see Eqs. (1)-(4)). CAFs produce a significant amount of fibers, resulting in a higher friction between different species, chosen to be proportional to the local amount of CAFs. High values of friction around the tumor nest prevent T-cells for penetrating the tumor in the spatial model.

The sample also contains diffusive signaling molecules that are at the origin of the immune activity. In the previous section, chemicals were not introduced, although they were associated with some coefficients of the dynamical system. Here, the chemicals that determine the cell behavior, are represented by a concentration c_j [50, 51]. Note that these chemicals have no mass and diffuse through the mixture with the diffusion coefficient D_c. For simplicity, we restrict ourselves to a single chemical of concentration c, that mediates both chemotaxis and activation of fibroblasts.

	δ_{CT}	α_{TC}	δ_{TF}	$\alpha_{NA,C}$	K_A
Control of:	Killing C-c by T-c	Attraction of T-c by C-c	Inhibition of T-c by F-c	Attraction of F-c to C-c	Activation of F-c
Efficient T-cells (T-c) but no attraction by (C-c)	$\delta\epsilon^{-1}$ ~ 10	ϵ^2 ~ 0.01	No role	No role	No role
Efficient T-cells but inhibited by (F-c)	$\delta\epsilon^{-1}$ ~ 10	ϵ ~ 0.1	$\delta\epsilon^{-1}$ ~ 10	1 ~ 1	δ ~ 1
Inefficient T-cells no need of fibroblasts	δ ≤ 1	ϵ ~ 0.1	No role	No role	No role
Efficient T-cells not inhibited by fibroblasts	$\delta\epsilon^{-1}$ ~ 10	ϵ ~ 0.1	δ ~ 1	1 ~ 1	δ ~ 1
Efficient T-cells and fibroblasts not attracted	$\delta\epsilon^{-1}$ ~ 10	ϵ ~ 0.1	$\delta\epsilon^{-1}$ ~ 10	ϵ ~ 0.1	δ ~ 1
Efficient T-cells fibroblasts not activated	$\delta\epsilon^{-1}$ ~ 10	ϵ ~ 0.1	$\delta\epsilon^{-1}$ ~ 10	ϵ ~ 0.1	$\delta\epsilon$ ~ 0.1

Table 2: Scaling variation and estimation of the numerical values for the coefficients entering in the model according to the different scenarios described in Section 3.2 and shown in Fig. 3. The coefficients above are those introduced in Eqs. (1)-(4). The left column summarizes the different roles that T-cells can play in a cell mixture and the values of the coefficients of the mixture are listed in the following horizontal line of the table. The scaling of δ is always 1, and $\alpha_{NA} \sim \delta\epsilon^4$.

The balance between its production and degradation rate writes $\tau_{cC}^{-1}\phi_C - \delta_c c$, since it is produced by cancer cells and naturally degraded. Within these considerations, we study the case where the tumor is well supplied with nutrients, which are therefore not explicitly mentioned, and write a set of conservation equations for each component of the mixture::

$$\begin{cases} \partial_t \phi_i + \nabla.(\phi_i \mathbf{v}_i) = \Gamma_i, \\ \partial_t c = D_c \nabla^2 c + \tau_{cC}^{-1}\phi_C - \delta_c c. \end{cases} \tag{8}$$

We now present a derivation for the average local velocity $\mathbf{v}_i$ of each species by deriving its momentum equation and the expressions for the various source terms.

4.1. Momentum and Free Energy Derivation

Considering that the dynamics is very slow and completely controlled by dissipation, the Onsager variational principle of least dissipation [52] yields the set of partial differential equations coupling the densities to the velocities in the mixture [48]. This principle, introduced by Lord Rayleigh and further developed by Onsager [53–56], is widely used in soft matter [57], in the biophysical context [43, 48, 52, 58, 59] as well as other areas of physics [60]. First we define a free energy $\mathcal{F}$ from a free energy density F and the associated chemical potentials μ_i, and a dissipation function $\mathcal{W}$:

$$\begin{cases} \mathcal{F} = \int d\mathbf{r}\, F(\{\phi_i\}, c) \quad ; \quad \mu_i = \frac{\delta \mathcal{F}}{\delta \phi_i}\,, \\ \mathcal{W} = \int \sum_{i\neq j} \frac{\xi_{ij}\phi_i\phi_j}{2} \left(\mathbf{v}_i - \mathbf{v}_j\right)^2 d\Omega\,, \end{cases}$$

where the ξ_{ij} are the relative friction coefficients between components i and j, and $\mathbf{v_i}$ and $\mathbf{v_j}$ are the velocities of the differenT-cell types. The Rayleighian is then defined as the sum of the dissipation function $\mathcal{W}$ and the rate of change of the free energy function $\mathcal{F}$. Within this framework, the final equations for the local velocities are obtained by minimizing the Rayleighian with respect to each velocity $\mathbf{v_i}$:

$$\mathcal{R} = \frac{d\mathcal{F}}{dt} + \mathcal{W}, \quad \frac{\delta \mathcal{R}}{\delta v_i} = 0 \Rightarrow \sum_j A_{ij}\mathbf{v}_j = -\nabla\mu_i\,,$$

where A_{ij} is the friction matrix and μ_i are the chemical potentials. Defining: $\tilde{\phi}_i = \phi_i\phi_0^{-1}$,the friction matrix reads:

$$\begin{cases} A_{ii} = \sum_{j\neq i,0}(\xi_{ij} + \xi_{j0}\tilde{\phi}_i)\phi_j + \xi_{i0}(1+\tilde{\phi}_i)^2\,, \\ A_{ij} = \phi_j(-\xi_{ij} + \xi_{i0}(1+\tilde{\phi}_i) + \xi_{j0}(1+\tilde{\phi}_j) \\ \qquad\qquad + \sum_{k\neq i,j,0}\xi_{k0}\tilde{\phi}_k). \end{cases}$$

Importantly, in our model we assume that all frictions ξ_{ij} are equal, except for the friction with the CAFs. In fact, the mass fraction of CAFs is assumed to reflect the amount of matrix produced by the fibroblasts, resulting in a very high friction in the medium. Therefore, we write: $\xi_{ij} = \xi_0, \xi_{iCAF} = \xi_0 + \xi_1\phi_{CAF}$.

After deriving the momentum equations, we construct the free energy density. Following [48] and inspired by the Cahn-Hilliard approach, we define a free energy density F as a sum of the interaction potential f and of the cost induced by the mass fractions gradients $\kappa(\nabla\phi_i)^2/2$. We also assume for f the Flory-Huggins free energy density of mixing and depends on the local mass fractions (or equivalently the volume fractions) of each component ϕ_i and on the concentration of the chemical c [61, 62]:

$$\begin{cases} F = f + \sum_{i,j}\frac{\kappa}{2}(\nabla\phi_i)^2;\ \mu_i = \partial f/\partial\phi_i - \kappa\nabla^2\phi_i\,, \\ f = \sum_i D_i\phi_i\log(\phi_i) - \sum_{i,j}\alpha_{ij}\phi_i\phi_j - \sum_i\beta_i\phi_i c\,. \end{cases} \tag{9}$$

The terms $D_i\phi_i\log(\phi_i)$ control both the diffusion and volume exclusion, the quadratic expansion $-\alpha_{ij}\phi_i\phi_j$ controls the attraction or repulsion between species, while the last term $-\beta_i\phi_i c$ is a chemo-attraction (or a chemo-repulsion) quantity mediated by

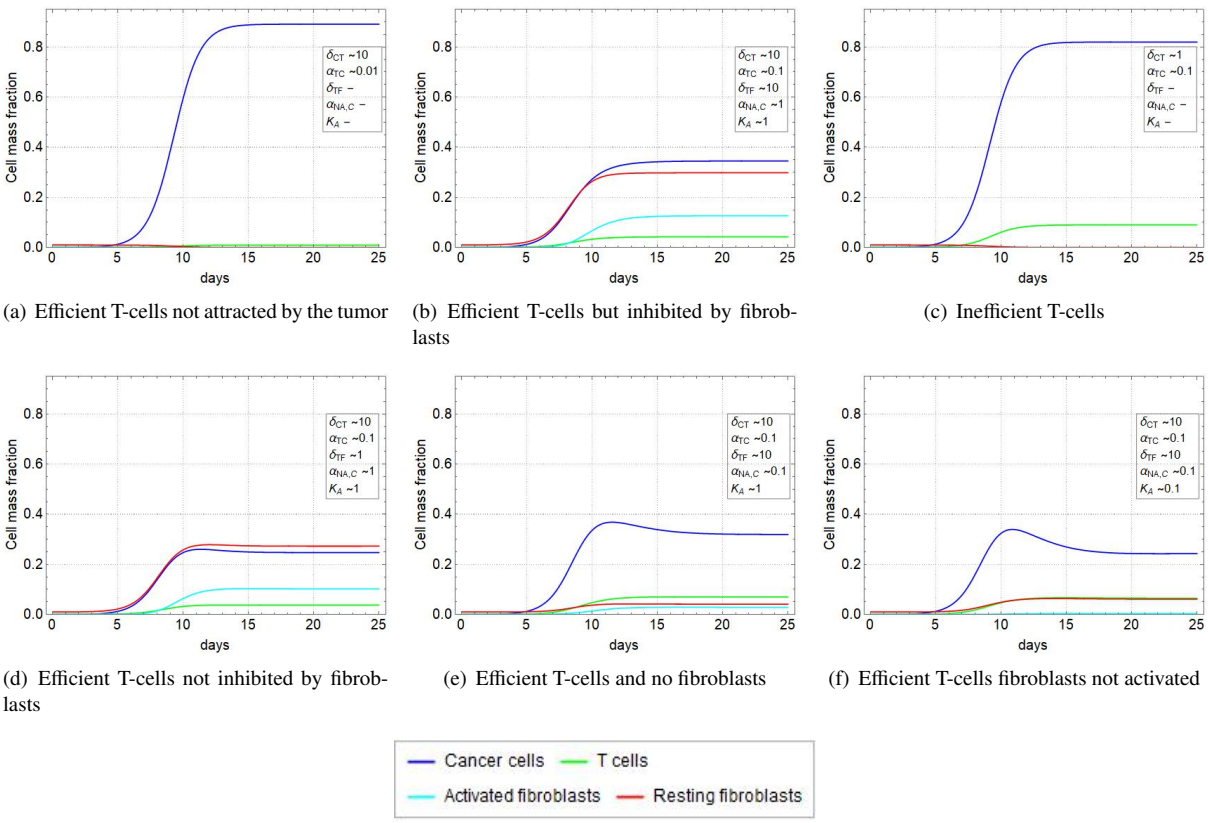

(a) Efficient T-cells not attracted by the tumor

(b) Efficient T-cells but inhibited by fibroblasts

(c) Inefficient T-cells

(d) Efficient T-cells not inhibited by fibroblasts

(e) Efficient T-cells and no fibroblasts

(f) Efficient T-cells fibroblasts not activated

Figure 3: With respect with the three scenarios shown in Fig. 1, different profiles are obtained from Eqs. (1)-(4) according to the derived set of parameters in Table. 2. **a**,**c**: Immune-desert tumor. Cancer cells proliferate when the immune response is inefficient or not attracted to the tumor. **b**: Immune-excluded tumor. CAFs barrier which inhibits T-cell infiltration, which promotes tumor growth. **d**, **e**, **f**: Immune-inflammed tumor. T-cell infiltration limits cancer cell growth.

the chemical c in the direction towards (or away from) the tumor nest.

In the following, we explain in more detail the effective free energy density of our system, as well as the expression of the different proliferation rates, and the values of the parameters, focusing on the attraction/repulsion and the chemotactic terms.

4.2. *Effective Free Energy Density and Source Terms*

We now apply the general formalism presented in the previous section to the cancer cell mixture using the same notation as Section 3 for C, T, F_{NA}, F_A. However, whereas in the first section these quantities represented averaged mass fractions over the whole tumor, here they are local mass fractions averaged over a small volume of the tumor but larger than the cell size. We now detail the effective free energy, focusing first on the interaction potential f defined in Eq. 9.

The attraction between cancer cells is represented by $-\lambda_{CC}C^2$, between cancer cells and T-cells by $-\lambda_{CT}CT$, and between all types of fibroblasts and cancer cells by $-\lambda_{CF}C(F_{NA} + F_A)$, where the λ coefficients are positive. These interactions are accounted for the free energy density that reads:

$$\begin{aligned} f = {} & D_C C \log(C) + D_T T \log(T) + D_{CAF} F_A \log(F_A) \\ & + D_{NA} F_{NA} \log(F_{NAF}) + D_0 \phi_0 \log(\phi_0) \\ & - \lambda_{CC} C^2 - \lambda_{CT} CT - \lambda_{CF} C(F_{NA} + F_A) \, . \end{aligned}$$

Finally, we focus on the proliferation rates to complete the system Eq. 8. Note that we must distinguish the cells produced *in situ*, such as the cancer cells C and the activated fibroblasts F_A, from the cells attracted to the tumor nest (T and F_{NA}) by the chemicals c. We keep the growth rate of cancer cells Γ_C given by Eq. 1 with $\delta_{TF} = 0$ because the inhibition of T-cells by fibroblasts is treated by increasing the friction created by the fiber barrier. T-cells and NAFs do not proliferate and are not derived from precursors at the tumor site, but are instead generated far away from the tumor and are attracted to it by chemotaxis. Thus, at the $\partial\Omega$ boundaries, their source rate is driven by an incoming flux due to the chemical c. For the NAFs, the volume term $\Gamma_{NA}|_\Omega$ does not include the source term $\alpha_{NA,C}$ (see Eq. 3) which is provided by the boundaries, and α_{NA} is neglected:

$$\begin{cases} \Gamma_T|_{\partial\Omega} = \frac{c(1-\mathcal{S})}{\tau_T} \quad \text{and} \quad \Gamma_T|_\Omega = -\delta T \mathcal{N}, \\ \Gamma_{NA}|_{\partial\Omega} = \frac{c(1-\mathcal{S})}{\tau_F} \text{ and } \Gamma_{NA}|_\Omega = -K_A F_{NA} C - \delta F_{NA} \mathcal{S}. \end{cases}$$

On the other hand, the production of CAFs is not changed and Γ_A defined in Eq. 4 is still relevant.

The parameter values are chosen so that the simulations mimic the different scenarios for the TME *in vivo*. We scale the different physical quantities in Table. 5. The spatial structure of the TME gives the different values for the free energy parameters. The dynamic parameters are related to those in the first part. For example, the tumor nest is a dense phase of cancer cells with mass fraction $C = 0.8$, but in the dilute phase $C \sim 0$, with an interface of size of order $d \sim 10\,\mu m$. This choice imposes the relative values of $D_C, D_0, \lambda_{CC}, \kappa$. Similarly, we assume a weak infiltration of T-cells and fibroblasts into the nest, resulting in low values for the attraction parameters $\lambda_{CT}, \lambda_{CF}$ when compared to λ_{CC}. Since D_{NAF}, D_{CAF}, D_T control the diffusion of the fibroblasts and T-cells, whose source is located at the boundaries, their values are determined by their density gradients between the boundaries and the tumor nest. At the same time, the time scale required for T-cells to kill the tumor nest is given by δ_{CT}, and the time scales for the arrival of the T-cells and NAFs into the domain, as well as their average mass fractions, are governed by τ_T, τ_F. The NAFs transform into CAFs in a time controlled by K. Scales for the values adopted in the model are based on values found in the literature and given in Table. 3 while the exact parameters introduced in the simulations are given in Table. 5. We use the letter d as time unit. One day is a typical division rate for cancer cells and for the eradication of tumor cells *in vitro* [63–65]. But the effective doubling times *in vivo* are longer [66]. In Table. 4, we present the parameters that we vary in the simulations shown in Fig. 4.

In the following, we will show that, once activated by tumor cells, fibroblasts can inhibit tumor growth through a confinement effect but also limit the cytotoxic role of T-cells or simply prevent their infiltration into the tumor.

4.3. Ambiguous Role of Fibroblasts in Tumorigenesis

To illustrate the ambiguous role of fibroblasts in tumor progression, we explore different scenarios through a 2-dimensional numerical study. This allows us to compare a fibrotic and a non-fibrotic tumor in the presence or absence of an immune response. Thus, the different growth cases we present are: a tumor without CAFs and T-cells, a tumor with both CAFs and T-cells, a tumor with T-cells but with a low level of CAFs, and a case with CAFs but no efficient T-cells. In the Appendix, we present other scenarios of free growth: a TME in the presence of only NAFs and inefficient T-cells (Fig. 1B), in presence of NAFs (Fig. 1C), and a TME in which only cancer cells are present (Fig. 1C). We first consider a single tumor nest before analyzing the case of two adjacent nests. Therefore, there is only one tumor nest at time $t = 0$ (Fig. 4A).

As shown in Fig. 4E,H (blue curve), in the case of a free-growing tumor, i.e. in the presence of NAFs and inactive T-cells, cancer cell growth is not hindered by any obstacles, so this is the most severe situation. However, the tumor provokes the formation of a stroma composed of the NAFs and inefficient T-cells. The presence of a stroma plays a role in the cancer cell growth described in Eq. 1 and leads to a growth that would be less important than in a case without stroma or composed only of NAFs (Fig. 1A→G). In fact, the pressure exerted by the stroma increases the mass fraction of cancer cells in the core of the nest, as well as the total mass fraction $\mathcal{N}$ at the stroma-nest interface. In the case of a free cancer growth without stroma, the tumor nest rapidly invades the environment and its surface fraction in the simulation window is almost 40% after 35 days, with a trend that is not yet saturated and an average mass fraction of cancer cells of 25%.

When fibroblasts are activated, they make the environment around the tumor nest fibrotic (Fig. 4B,C), with a mass fraction around the nest reaching 20-30%. As explained earlier in Section 4.1, the fibers in our model are introduced by an increase of the friction coefficient between the different species and the activated fibroblasts, which is directly related to the fiber concentration. The tumor cells are then trapped behind a barrier with a very high friction which prevents the nest from expanding, and the surface area of the tumor nest decreases to 25% after 35 days, with a fibrotic area reaching 70%, while the average cancer cell decreases to 17% (Fig. 4E-F-G cyan curve). The fibroblast population is composed of 30% NAFs and 70% CAFs, as the average fibroblast mass fraction is 26% (Fig. 4I-K cyan curve).

At the same time, even in a situation where T-cells are efficient, the barrier precludes T-cells from the tumor (Fig. 4C). In the latter case, tumor integrity is maintained and CAFs play a tumor-promoting role, inhibiting the immune response and stabilizing the tumor nest at 7.5% of the domain, with a fibrotic zone of 50% (Fig. 4E-F-H,green curve). In this scenario, the average mass fractions are 5% for cancer cells, 10% for CAFs, 10% for NAFs (so 20% for the fibroblast population) and 20% for T-cells. It is interesting to note that this scenario quickly leads to a stable steady state. In contrast, the other simulations take longer times to reach a steady state. This could be due to the fact that the stroma builds up quickly compared to cell death when the cell population is not renewed, and that the steady state corresponds to a small nest that is reached after a short period of growth.

When T-cells are introduced without transformation from NAFs to CAFs (Fig. 4I-red curve), the tumor dies as cancer cells are eliminated and the compact nest disappears (Fig. 4E-red curve). As the stroma initially builds up due to the presence of a tumor, the fibroblast and T-cell populations slowly relax. However, the tumor stroma takes a long time to retract. This suggests that even if the cancer is cured, the effects on the tissue can be long-lasting. In this case of non-activation of NAFs, T-cells infiltrate the core of the nest thanks

Parameter	meaning	value	Ref
τ	typical timescale	$1\,d$	[63]
L	alveola typical size	$10^2\,\mu m$	[7]
ξ	friction	$10^4\,kg.\mu m^{-3}.d^{-1}$	[48]
f_0	energy density	$10^6\,kg.\mu m^{-1}.d^{-2}$	[48]
$\sqrt{\kappa}/f_0$	interface size	$10\,\mu m$	[48]

Table 3: Different scaling in the spatial model

Parameter	free-growth	immune desert	immune excluded	immune inflamed
δ_{CT}	$5\times10^{-3}\,d^{-1}$	$5\times10^{-3}\,d^{-1}$	$5\,d^{-1}$	$5\,d^{-1}$
K	$10^{-2}\,d^{-1}$	$10\,d^{-1}$	$10\,d^{-1}$	$10^{-2}\,d^{-1}$

Table 4: Values of the parameters varying according to the different scenarios for tumor infiltration

Parameter	value
D_0	$10^6\,kg.\mu m^{-1}.d^{-2}$
D_C	$1\times10^5\,kg.\mu m^{-1}.d^{-2}$
D_T, D_{NAF}, D_{CAF}	$2.5\times10^5\,kg.\mu m^{-1}.d^{-2}$
λ_{CC}	$1.25\times10^6\,kg.\mu m^{-1}.d^{-2}$
λ_{CT}	$7.5\times10^5\,kg.\mu m^{-1}.d^{-2}$
λ_{CF}	$0\,kg.\mu m^{-1}.d^{-2}$
κ	$3.6\times10^7\,kg.\mu m.d^{-2}$
δ	$1.18\,d^{-1}$
δ_{CT}	$5\,d^{-1}$
τ_T, τ_{NA}	$2.5\times10^{-3}\,\mu m.d^{-1}$
K	$10\,d^{-1}$
ξ_0	$3\times10^2\,kg.\mu m^{-3}.d^{-1}$
ξ_1	$3\times10^5\,kg.\mu m^{-3}.d^{-1}$

Table 5: Selected values of the parameters in the spatial model

to the attraction of cancer cells (through the parameter λ_{CT}) and allows tumor reduction (Fig. 4D). Therefore, their invasion is efficient only in the absence of fibers. (Fig. 4G-red curve).

There are many mechanisms able to inhibit the immune system. In addition to the exclusion of T-cells from the tumor and the absence of active feedback, low attractiveness can also reduce the immune response. Indeed, when T-cells are less attracted, for example because chemotaxis is not efficient enough, the tumor is free to expand. In Fig. 4B, the cytotoxicity of T-cells is impaired, but their chemotaxis from the boundaries of the domains is not. This leads to an accumulation of inefficient T-cells around the tumor nest.

Next, we analyze the case where two tumor nests are nucleated and their mutual interactions. We assume that that they have the same initial size and mass fraction of cancer cells. In the absence of CAFs, an immune response is triggered and T-cell infiltration can occur. As expected, in the immune-inflamed tumor, the activity of T-cells reduces the ability of the two nests to coalesce by also reducing their mass fraction, leading to very low values of cancer cells (see Fig. 5A). When T-cell activity is marginalized by the presence of CAFs, the two nests slowly coalesce to form a single solid tumor nest (see Fig. 5B). In this case, growth is actually limited by the tumor-promoting function of CAFs. Although, fibroblasts surround the tumor, but they do not inhibit its growth which is enhanced due to the lack of immune cells inside the nuclei. On the contrary, in the absence of T-cells chemotaxis, the tumor growth is unrestricted and the nests create a larger tumor by also increasing their mass fraction (see Fig. 5C). In the latter cases, coalescence leads to anisotropic shapes of the tumor. Although relaxation in our model eventually leads to a round shape, this relaxation is slower for large tumors and even more for fibrotic tumors where friction significantly slows down this process. Patterns associated with coalescence may thus provide insight into the interpretation of anisotropic patterns in tumors. These are also related to the particular geometry of the system, such as the shape of the organ and the location of various blood vessels (see Appendix).

5. Conclusions

Our work provides a physical model to quantify the role of the immune system in human lung tumors. The focus is on early tumor growth prior to angionesis and the development of its stroma rich in T-cells and fibroblasts, the activation of non-activated fibroblasts into cancer-associated fibroblasts and the marginalization of T-cells from the tumor nest. Other immune cells, such as macrophages, could complete this study in a further study.

After analyzing the data from the literature and from patients with LUSC or LUAD pathologies, we proposed a physical model, both theoretical and numerical, for the interactions between cancer cells, T-cells and fibroblasts during tumor progression and their different roles. In particular, fibroblasts are introduced in the model in their inactive and active states (NAFs and CAFs). The modeling involves two steps: firstly, a dynamic study aimed at elucidating the key factors that can characterize the properties of the microenvironment on which the ability of T-cells to inhibit tumor growth depends. Scenarios scaled by only two parameters control the dynamics and evaluate the aggressiveness of the tumor. In particular, we established the spatial organization of the differenT-cell types inside and outside the tumor core. The model was based on the continuous mixture model derived from Onsager's variational principle. Simulations were performed with the FEM software COMSOL Multiphysics in a two-dimensional framework. This provided a complete description of the tumor morphology and composition. In fact, we explored different scenarios to fully appreciate the role of all cell types involved. The results confirmed the experimental evidence that CAFs play a dual role in promoting and suppressing cancer cell proliferation. First, they alter the tumor microenvironment with a fiber barrier that reduces the motility and activity of

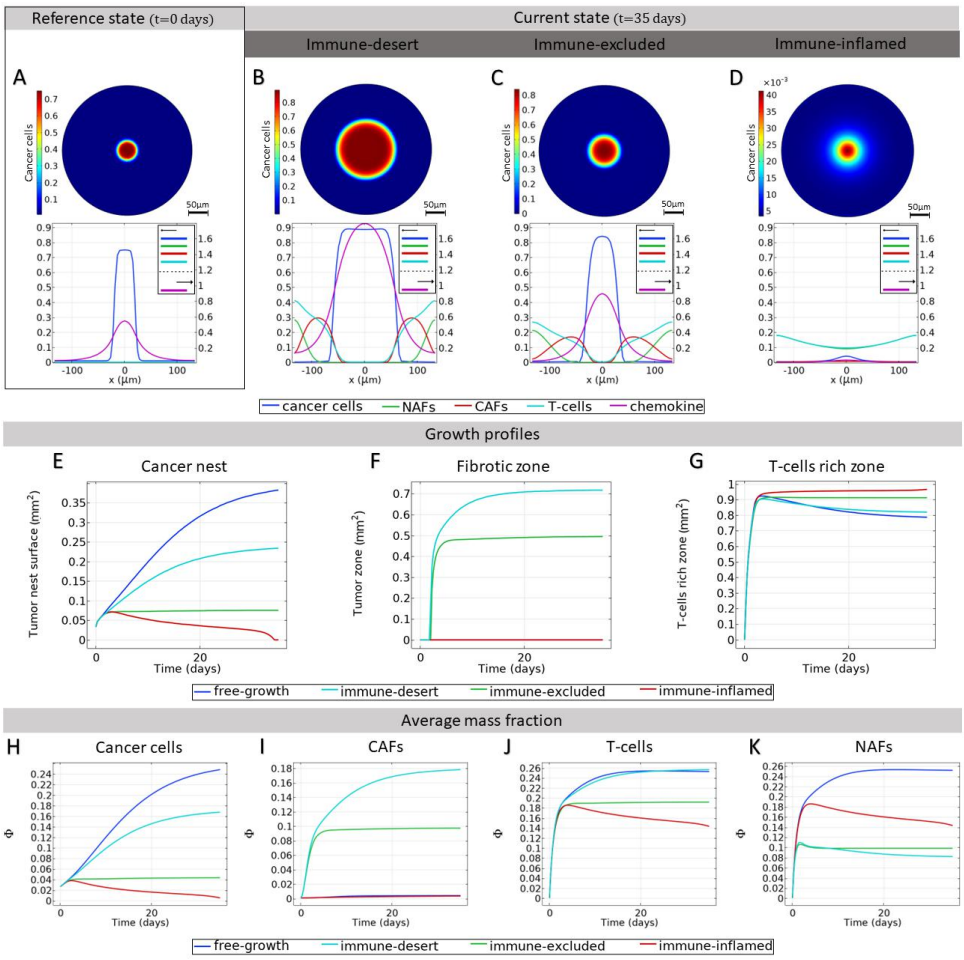

Figure 4: Small solid tumor growth. We refer here to different tumor phenotypes in Fig.1. **A**: Mass fraction of cancer cells at time $t = 0$ days and profile of different mass fractions on a section of the tumor. **B-C-D**: Mass fraction of cancer cells at time $t = 35$ days and profile of mass fraction in immunodeficient tumor (**B**), when immune infiltration is inhibited by CAFs (**C**), and in immune-inflamed tumor (**D**). **E-F-G**: We show the development of different zones. **E**: Surface fraction profile of the tumor nest for different scenarios, calculated as $S/S_{total} = \int d\mathbf{r}\delta(C > 0.1)/S_{total}$. **F**: Fibrotic surface fraction profile for different scenarios, calculated as $S/S_{total} = \int d\mathbf{r}\delta(CAF > 0.1)/S_{total}$. **G**: T-cell rich area fraction profile for different scenarios, calculated as $S = \int d\mathbf{r}\delta(T > 0.1)/S_{total}$. **H**: Cancer cell average mass fractions. **I**: CAFs average mass fractions. **J**: T-cell average mass fractions. **K**: Nafs average mass fractions.

T-cells, thereby promoting cancer cell growth. At the same time, this growth is limited and lower than in the absence of active fibroblasts. Moreover, we have also shown that although the different parameters can take a wide range of values and continuously change the results of the numerical study, different scenarios can be drawn by looking only at the orders of magnitude.

In this study, we did not consider the fibers of the extracellular matrix as a component *per se*, but we considered them through the friction increase. An extension of this modeling would be to include anisotropic friction due to a nematic field, as done in Ref. [67], where the nematic fields, the fibroblasts and the fibronectin cause anisotropic friction.

Our physical model aims to limit the number of parameters as much as possible. This may seem far-fetched given the complexity of the biological system, especially in vivo. However, there are several reasons for this limitation. First, determining the range of values for these parameters is a complex task in the absence of direct measurement. The strategy we used in Section. 3 is to isolate each process corresponding to each parameter and thus construct the model step by step. In Section. 4.1 we used both this latter strategy and the spatial structure of the mixing. In addition, the different combination of the parameters' values provide a wide variety of scenarios and it would be sufficient to modify these values to model new chemical entering the system. Limiting the complexity of the different processes allows us to focus on other aspects of the problem, such as the time evolution and the spatial structure, as well as a more precise quantitative study. In the same spirit, we numerically report in Section. 4.1 a 2-dimensional system without substrate, which yields results that we can consider similar as a 3-dimensional system with an invariance in the third dimension.

In conclusion, this numerical investigation may help to understand the limitations of the immune system in the face of solid tumor growth. Understanding

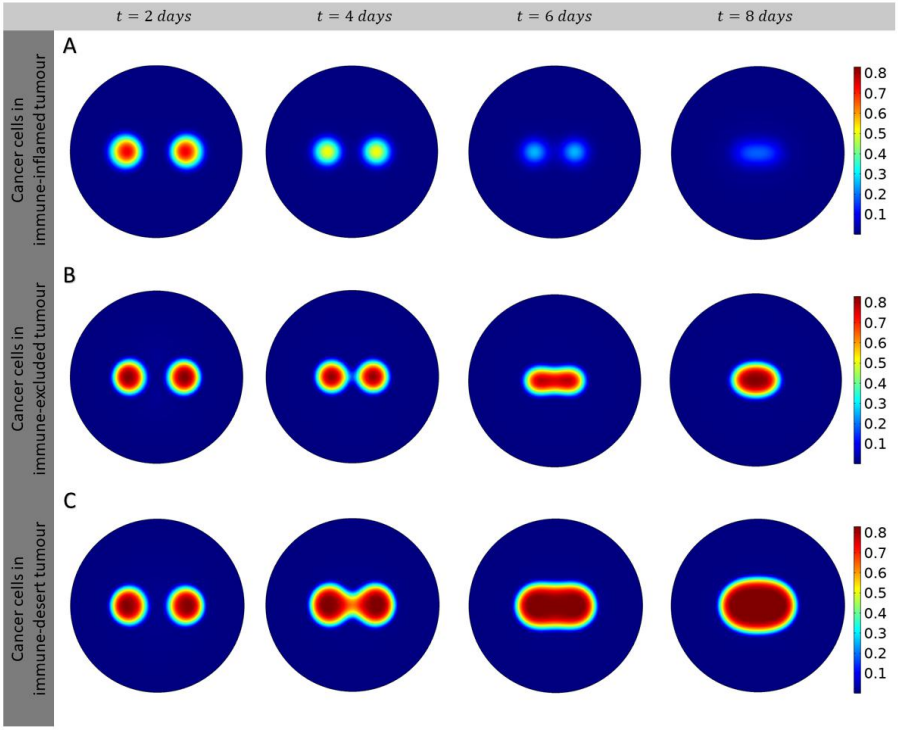

Figure 5: Growth process of two small solid tumors: density plots showing cancer cell population. We start with two tumor nests placed at the same distance from the center of the domain ($30\mu m$), sharing the same mass fraction of cancer cells and we present different scenarios. **A**: Nests in immune-inflamed tumor. **B**: Nests interacting in immune-excluded tumor, with chemotactic T-cells and CAFs. **C**: Nests coalescencing in immune-desert tumor, i.e. in the presence of inefficient T-cells.

how immune cells are excluded from the tumor nest may be helpful in the drug design of T-cell-based therapies. Conversely, the numerical reproduction of various processes that can be observed *in vivo* is an important step in the context of personalized medicine. A next step in the theoretical and numerical investigation would therefore be to introduce drug molecules into the framework we have presented. Finally, it would be interesting to extend our model to follow the tumor from the alveolar stage of the lung within a 3-dimensional description.

Appendix

In this appendix, we show cases of free growth but in simpler stroma: the case of a stroma composed by NAFs and inefficient T-cells (Fig. Sup. 1-B), a stroma composed by NAFs only (Fig. Sup. 1-C), and the case without stroma (Fig. Sup. 1-D), the tumor nest surface fraction in the simulation window for the different scenarios (Fig. Sup 1-E), and the average mass fraction of the cancer cells and the NAFs (Fig. Sup 1-F,G). The values of the parameters depending on the scenario are shown in Table. Sup 1.

Besides, we show the evolution of the tumor in the case with efficient T-cells and NAFs without CAFs (Fig. Sup 1-H).

We also obtain different configurations by assuming deformed domains in order to study the anisotropic response of the tumor stroma (Fig. Sup. 2-A-B). In particular, the results obtained differ from those presented above by introducing T-cells and NAFs only from the upper side of the boundaries, this assuming the possibility that T-cells are able to reach the nest from different parts. Finally, different regions have been highlighted: in *light blue* the cancer cells nest, in *red* the barrier of activated fibroblasts and in *green* the healthy stroma composed of NAFs and T-cells.

Parameter	τ_T ($\mu m.d^{-1}$)	τ_{NAF} ($\mu m.d^{-1}$)
C-c+NAFs+inefficient T-cells	2.5×10^{-3}	2.5×10^{-3}
C-c+NAFs	2.5×10^{-6}	2.5×10^{-3}
C-c	2.5×10^{-6}	2.5×10^{-6}

Table. Sup 1: Parameter values varying depending on the scenario

Author contributions

M.BA and J.A conceived and designed the project, built the physical model and the theoretical analysis. H.S and P.S provided the biological data and images. C.B and J.A performed the numerical simulations. M.F assisted the implementation of the simulations. M.BA and J.A wrote the manuscript with input from C.B, P.S, H.S, and M.F.

Data and materials availability

All data are available in the main text, in the figures and in the tables. Comsol Multiphysics files and raw

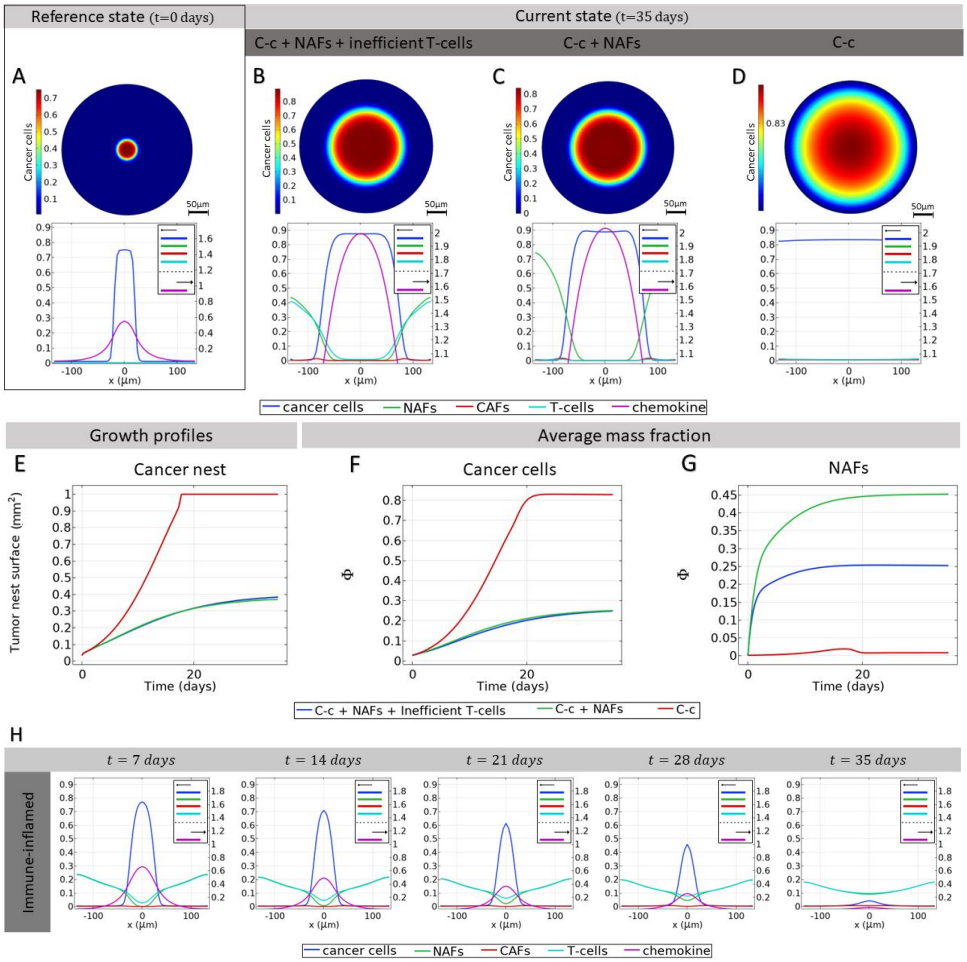

Figure. Sup 1: **A**-**G**: Cancer population density plots for different scenarios: Cancer cells (C-c)+NAFs+Inefficient T-cells, Cancer cells+NAFs,Cancer cells alone. **A**: Mass fraction of cancer cells at time $t = 0$ days and profile of different mass fractions on a section of the tumor. **B**: Mass fraction of cancer cells at time $t = 35$ days and mass fraction profile for a case of a stroma composed by C-c, NAFs, and inefficient T-cells. **C**: Mass fraction of cancer cells at time $t = 35$ days and profile of the different mass fractions on a cut of the tumor for a case of a stroma composed by C-c and NAFs. **D**: Mass fraction of cancer cells at time $t = 35$ days and mass fraction profile for a case with no stroma in the tumor microenvironment. **E**: Surface fraction of the tumor nest in the different scenarios. **F**: Average mass fraction of the cancer cells in the different scenarios. **G**: Average mass fraction of the NAFs in the different scenarios. **H**: Time evolution of the mass fraction profile of the cut of the simulation window in the case of a tumor in the presence of efficient T-cells and NAFs only, without T-cells.

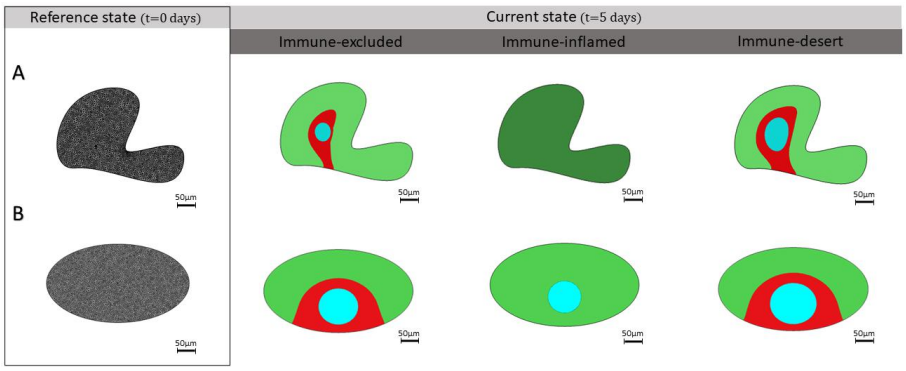

Figure. Sup 2: Different tumor phenotypes in non-spherical domains. Deformed shapes result in anisotropic configurations by forcing NAFs and T-cells to enter the domain from only one side of the boundary. Different colors indicate separated regions where the nest (in light blue) is confined by the boundary of CAFs (in red) within a healthy stroma (in green). **A**: Immune-inflamed case leads to disappearance cancer cells in 5 days. **B**: Elliptical area leads to slower dynamics.

data used in this work are available upon request.

Declaration of interests

The authors declare that they have no known competing financial interests or personal relationships that could have appeared to influence the work reported in this paper.

Acknowledgements

M.BA and H.S acknowledge the financial support from ITMO Cancer of Aviesan within the framework of the 2021-2030 Cancer Control Strategy, on funds administrated by Inserm (PCSI 2021,MCMP 2022). J.A acknowledges the financial support from ANR COLLAMOEBOID (ANR-20-CE13-0031). C.B acknowledges the Italian Ministry of Universities and Research (MUR) for the project DICAM-EXC, University of Trento, Departments of Excellence 2023-2027 (grant DM 230/2022). We thank Philippe Benaroch, Layla Mathieson, Xudong Xing for useful discussions.

References

[1] J. Wu, C. Liang, M. Chen, W. Su, Association between tumor-stroma ratio and prognosis in solid tumor patients: a systematic review and meta-analysis, Oncotarget 7 (42) (2016) 68954.

[2] H. Sung, J. Ferlay, R. L. Siegel, M. Laversanne, I. Soerjomataram, A. Jemal, F. Bray, Global cancer statistics 2020: Globocan estimates of incidence and mortality worldwide for 36 cancers in 185 countries, CA: a cancer journal for clinicians 71 (3) (2021) 209–249.

[3] R. D. Schreiber, L. J. Old, M. J. Smyth, Cancer immunoediting: integrating immunity's roles in cancer suppression and promotion, Science 331 (6024) (2011) 1565–1570.

[4] L. M. Coussens, Z. Werb, Inflammation and cancer, Nature 420 (6917) (2002) 860–867.

[5] L. Mathieson, L. Koppensteiner, S. Pattle, D. A. Dorward, R. O'Connor, A. R. Akram, Subpopulations of cancer-associated fibroblasts expressing fibroblast activation protein and podoplanin in non-small cell lung cancer are a predictor of poor clinical outcome, bioRxiv (2022) 2022–09.

[6] M. Mukherjee, O. Chepizhko, M. C. Lionetti, S. Zapperi, C. A. La Porta, H. Levine, Infiltration of tumor spheroids by activated immune cells, bioRxiv (2022).

[7] J. A. Grout, P. Sirven, A. M. Leader, S. Maskey, E. Hector, I. Puisieux, F. Steffan, E. Cheng, N. Tung, M. Maurin, et al., Spatial positioning and matrix programs of cancer-associated fibroblasts promote t-cell exclusion in human lung tumors, Cancer Discovery 12 (11) (2022) 2606–2625.

[8] H. Salmon, R. Remark, S. Gnjatic, M. Merad, Host tissue determinants of tumour immunity, Nature Reviews Cancer 19 (4) (2019) 215–227.

[9] H. F. Dvorak, Tumors: wounds that do not heal, New England Journal of Medicine 315 (26) (1986) 1650–1659.

[10] N. Nakamura, T. Iijima, K. Mase, S. Furuya, J. Kano, Y. Morishita, M. Noguchi, Phenotypic differences of proliferating fibroblasts in the stroma of lung adenocarcinoma and normal bronchus tissue, Cancer science 95 (3) (2004) 226–232.

[11] W. Wang, Q. Li, T. Yamada, K. Matsumoto, I. Matsumoto, M. Oda, G. Watanabe, Y. Kayano, Y. Nishioka, S. Sone, et al., Crosstalk to stromal fibroblasts induces resistance of lung cancer to epidermal growth factor receptor tyrosine kinase inhibitorsfibroblasts induce egfr-tki resistance, Clinical Cancer Research 15 (21) (2009) 6630–6638.

[12] Q. Peng, L. Zhao, Y. Hou, Y. Sun, L. Wang, H. Luo, H. Peng, M. Liu, Biological characteristics and genetic heterogeneity between carcinoma-associated fibroblasts and their paired normal fibroblasts in human breast cancer, PLoS One 8 (4) (2013) e60321.

[13] R. Kalluri, The biology and function of fibroblasts in cancer, Nature Reviews Cancer 16 (9) (2016) 582–598.

[14] R. Barrett, E. Puré, Fibrroblasts: key determinants of tumor immunity and immunotherapy, Current opinion in immunology 64 (2020) 80–87.

[15] H. Salmon, K. Franciszkiewicz, D. Damotte, M.-C. Dieu-Nosjean, P. Validire, A. Trautmann, F. Mami-Chouaib, E. Donnadieu, et al., Matrix architecture defines the preferential localization and migration of t cells into the stroma of human lung tumors, The Journal of clinical investigation 122 (3) (2012) 899–910.

[16] L. B. Yaegashi, C. M. Baldavira, T. G. Prieto, J. Machado-Rugolo, A. P. P. Velosa, L. K. R. Da Silveira, A. Assato, A. M. Ab'Saber, R. Falzoni, T. Takagaki, et al., In situ overexpression of matricellular mechanical proteins demands functional immune signature and mitigates non-small cell lung cancer progression, Frontiers in Immunology (2021) 3199.

[17] G. Cheng, J. Tse, R. K. Jain, L. L. Munn, Micro-environmental mechanical stress controls tumor spheroid size and morphology by suppressing proliferation and inducing apoptosis in cancer cells, PLoS one 4 (2) (2009) e4632.

[18] J. Barbazan, C. Pérez-González, M. Gómez-González, M. Dedenon, S. Richon, E. Latorre, M. Serra, P. Mariani, S. Descroix, P. Sens, et al., Cancer-associated fibroblasts actively compress cancer cells and modulate mechanotransduction, Nature Communications 14 (1) (2023) 6966.

[19] M. R. Nazareth, L. Broderick, M. R. Simpson-Abelson, R. J. Kelleher, S. J. Yokota, R. B. Bankert, Characterization of human lung tumor-associated fibroblasts and their ability to modulate the activation of tumor-associated t cells, The Journal of Immunology 178 (9) (2007) 5552–5562.

[20] M. A. Lakins, E. Ghorani, H. Munir, C. P. Martins, J. D. Shields, Cancer-associated fibroblasts induce antigen-specific deletion of cd8+ t cells to protect tumour cells, Nature communications 9 (1) (2018) 1–9.

[21] K. Hiraoka, M. Miyamoto, Y. Cho, M. Suzuoki, T. Oshikiri, Y. Nakakubo, T. Itoh, T. Ohbuchi, S. Kondo, H. Katoh, Concurrent infiltration by cd8+ t cells and cd4+ t cells is a favourable prognostic factor in non-small-cell lung carcinoma, British journal of cancer 94 (2) (2006) 275–280.

[22] C. Liu, L. Yang, H. Xu, S. Zheng, Z. Wang, S. Wang, Y. Yang, S. Zhang, X. Feng, N. Sun, et al., Systematic analysis of il-6 as a predictive biomarker and desensitizer of immunotherapy responses in patients with non-small cell lung cancer, BMC medicine 20 (1) (2022) 1–15.

[23] P. Gueguen, C. Metoikidou, T. Dupic, M. Lawand, C. Goudot, S. Baulande, S. Lameiras, O. Lantz, N. Girard, A. Seguin-Givelet, et al., Contribution of resident and circulating precursors to tumor-infiltrating cd8+ t cell populations in lung cancer, Science Immunology 6 (55) (2021) eabd5778.

[24] C. E. Brown, R. P. Vishwanath, B. Aguilar, R. Starr, J. Najbauer, K. S. Aboody, M. C. Jensen, Tumor-derived chemokine mcp-1/ccl2 is sufficient for mediating tumor tropism of adoptively transferred t cells, The Journal of Immunology 179 (5) (2007) 3332–3341.

[25] J. Sieren, J. Weydert, A. Bell, B. De Young, A. Smith, J. Thiesse, E. Namati, G. McLennan, An automated segmentation approach for highlighting the histological complexity of human lung cancer, Annals of biomedical engineering 38 (12) (2010) 3581–3591.

[26] J. Sieren, A. Smith, J. Thiesse, E. Namati, E. Hoffman, J. Kline, G. McLennan, Exploration of the volumetric composition of human lung cancer nodules in correlated histopathology and computed tomography, Lung Cancer 74 (1) (2011) 61–68.

[27] D. Lambrechts, E. Wauters, B. Boeckx, S. Aibar, D. Nittner, O. Burton, A. Bassez, H. Decaluwé, A. Pircher, K. Van den Eynde, et al., Phenotype molding of stromal cells in the

lung tumor microenvironment, Nature medicine 24 (8) (2018) 1277–1289.

[28] A. S. Ireland, A. M. Micinski, D. W. Kastner, B. Guo, S. J. Wait, K. B. Spainhower, C. C. Conley, O. S. Chen, M. R. Guthrie, D. Soltero, et al., Myc drives temporal evolution of small cell lung cancer subtypes by reprogramming neuroendocrine fate, Cancer cell 38 (1) (2020) 60–78.

[29] N. Kim, H. K. Kim, K. Lee, Y. Hong, J. H. Cho, J. W. Choi, J.-I. Lee, Y.-L. Suh, B. M. Ku, H. H. Eum, et al., Single-cell rna sequencing demonstrates the molecular and cellular reprogramming of metastatic lung adenocarcinoma, Nature communications 11 (1) (2020) 2285.

[30] A. M. Laughney, J. Hu, N. R. Campbell, S. F. Bakhoum, M. Setty, V.-P. Lavallee, Y. Xie, I. Masilionis, A. J. Carr, S. Kottapalli, et al., Regenerative lineages and immune-mediated pruning in lung cancer metastasis, Nature medicine 26 (2) (2020) 259–269.

[31] A. Maynard, C. E. McCoach, J. K. Rotow, L. Harris, F. Haderk, D. L. Kerr, A. Y. Elizabeth, E. L. Schenk, W. Tan, A. Zee, et al., Therapy-induced evolution of human lung cancer revealed by single-cell rna sequencing, Cell 182 (5) (2020) 1232–1251.

[32] J. Qian, S. Olbrecht, B. Boeckx, H. Vos, D. Laoui, E. Etlioglu, E. Wauters, V. Pomella, S. Verbandt, P. Busschaert, et al., A pan-cancer blueprint of the heterogeneous tumor microenvironment revealed by single-cell profiling, Cell research 30 (9) (2020) 745–762.

[33] X. Xing, F. Yang, Q. Huang, H. Guo, J. Li, M. Qiu, F. Bai, J. Wang, Decoding the multicellular ecosystem of lung adenocarcinoma manifested as pulmonary subsolid nodules by single-cell rna sequencing, Science advances 7 (5) (2021) eabd9738.

[34] N. K. Altorki, A. C. Borczuk, S. Harrison, L. K. Groner, B. Bhinder, V. Mittal, O. Elemento, T. E. McGraw, Global evolution of the tumor microenvironment associated with progression from preinvasive invasive to invasive human lung adenocarcinoma, Cell reports 39 (1) (2022) 110639.

[35] Curated cancer cell atlas collected, annotated and analyzed cancer scrna-seq datasets , weizmann institute of science, `https://www.weizmann.ac.il/sites/3CA/lung`, accessed: 2023-03-30.

[36] M. Hosokawa, H. Kenmotsu, Y. Koh, T. Yoshino, T. Yoshikawa, T. Naito, T. Takahashi, H. Murakami, Y. Nakamura, A. Tsuya, et al., Size-based isolation of circulating tumor cells in lung cancer patients using a microcavity array system, PloS one 8 (6) (2013) e67466.

[37] Y. Mitsui, E. L. Schneider, Relationship between cell replication and volume in senescent human diploid fibroblasts, Mechanisms of ageing and development 5 (1976) 45–56.

[38] H. Tasnim, G. M. Fricke, J. R. Byrum, J. O. Sotiris, J. L. Cannon, M. E. Moses, Quantitative measurement of naïve t cell association with dendritic cells, frcs, and blood vessels in lymph nodes, Frontiers in immunology 9 (2018) 1571.

[39] E. L. Bearer, J. S. Lowengrub, H. B. Frieboes, Y.-L. Chuang, F. Jin, S. M. Wise, M. Ferrari, D. B. Agus, V. Cristini, Multiparameter computational modeling of tumor invasion, Cancer research 69 (10) (2009) 4493–4501.

[40] V. Cristini, H. B. Frieboes, R. Gatenby, S. Caserta, M. Ferrari, J. Sinek, Morphologic instability and cancer invasion, Clinical Cancer Research 11 (19) (2005) 6772–6779.

[41] V. Cristini, X. Li, J. S. Lowengrub, S. M. Wise, Nonlinear simulations of solid tumor growth using a mixture model: invasion and branching, Journal of mathematical biology 58 (4-5) (2009) 723.

[42] Y. L. Huang, C. Shiau, C. Wu, J. E. Segall, M. Wu, The architecture of co-culture spheroids regulates tumor invasion within a 3d extracellular matrix, Biophysical reviews and letters 15 (03) (2020) 131–141.

[43] T. Balois, M. Ben Amar, Morphology of melanocytic lesions in situ, Scientific reports 4 (2014) 3622.

[44] E. J. Koay, Y. Lee, V. Cristini, J. S. Lowengrub, Y. Kang, F. A. San Lucas, B. P. Hobbs, R. Ye, D. Elganainy, M. Almahariq, et al., A visually apparent and quantifiable ct imaging feature identifies biophysical subtypes of pancreatic ductal adenocarcinoma, Clinical Cancer Research 24 (23) (2018) 5883–5894.

[45] L. Li, W. B. Neaves, Normal stem cells and cancer stem cells: the niche matters, Cancer research 66 (9) (2006) 4553–4557.

[46] B. Psaila, D. Lyden, The metastatic niche: adapting the foreign soil, Nature Reviews Cancer 9 (4) (2009) 285–293.

[47] Y. Liu, X. Cao, Characteristics and significance of the pre-metastatic niche, Cancer cell 30 (5) (2016) 668–681.

[48] J. Ackermann, M. Ben Amar, J.-F. Joanny, Multi-cellular aggregates, a model for living matter, Physics Reports 927 (2021) 1–29.

[49] COMSOL Multiphysics® v. 6.2. www.comsol.com. COMSOL AB, Stockholm, Sweden.

[50] F. Olmeda, M. Ben Amar, Clonal pattern dynamics in tumor: The concept of cancer stem cells, Scientific Reports 9 (1) (2019) 15607.

[51] L. Mori, M. Ben Amar, Stochasticity and drug effects in dynamical model for cancer stem cells, Cancers 15 (3) (2023) 677.

[52] J. Ackermann, M. Ben Amar, Onsager's variational principle in proliferating biological tissues, in presence of activity and anisotropy, Eur. Phys. J. Plus (2023) 138:1103.

[53] J. W. Strutt, Some general theorems relating to vibrations, Proceedings of the London Mathematical Society 1 (1) (1871) 357–368.

[54] L. Onsager, Reciprocal relations in irreversible processes. i., Physical review 37 (4) (1931) 405.

[55] L. Onsager, Reciprocal relations in irreversible processes. ii., Physical review 38 (12) (1931) 2265.

[56] L. Onsager, S. Machlup, Fluctuations and irreversible processes, Physical Review 91 (6) (1953) 1505.

[57] M. Doi, Onsager's variational principle in soft matter, Journal of Physics: Condensed Matter 23 (28) (2011) 284118.

[58] H. Wang, T. Qian, X. Xu, Onsager's variational principle in active soft matter, Soft Matter 17 (13) (2021) 3634–3653.

[59] H. B. da Rocha, J. Bleyer, H. Turlier, A viscous active shell theory of the cell cortex, Journal of the Mechanics and Physics of Solids 164 (2022) 104876.

[60] E. Minguzzi, Rayleigh's dissipation function at work, European Journal of Physics 36 (3) (2015) 035014.

[61] P. J. Flory, Thermodynamics of high polymer solutions, The Journal of Chemical Physics 10 (1) (1942) 51–61.

[62] M. L. Huggins, Solutions of long chain compounds, The Journal of Chemical Physics 9 (5) (1941) 440–440.

[63] Cellosaurus - a knowledge resource on cell lines, https://www.cellosaurus.org, Accessed: 2023-12-21.

[64] Y. Xie, A. Akpinarli, C. Maris, E. L. Hipkiss, M. Lane, E.-K. M. Kwon, P. Muranski, N. P. Restifo, P. A. Antony, Naive tumor-specific cd4+ t cells differentiated in vivo eradicate established melanoma, Journal of Experimental Medicine 207 (3) (2010) 651–667.

[65] C. C. Kloss, M. Condomines, M. Cartellieri, M. Bachmann, M. Sadelain, Combinatorial antigen recognition with balanced signaling promotes selective tumor eradication by engineered t cells, Nature biotechnology 31 (1) (2013) 71–75.

[66] H. T. Winer-Muram, S. G. Jennings, R. D. Tarver, A. M. Aisen, M. Tann, D. J. Conces, C. A. Meyer, Volumetric growth rate of stage i lung cancer prior to treatment: serial ct scanning, Radiology 223 (3) (2002) 798–805.

[67] C. Jacques, J. Ackermann, S. Bell, C. Hallopeau, C. Perez-Gonzalez, L. Balasubramaniam, X. Trepat, B. Ladoux, A. Maitra, R. Voituriez, et al., Aging and freezing of active nematic dynamics of cancer-associated fibroblasts by fibronectin matrix remodeling, bioRxiv (2023) 2023–11.